Optics Letters

Programmable hyperspectral coherent anti-Stokes Raman scattering microscopy

Janet E. Sorrells,[1,2] Lingxiao Yang,[1,3] Rishyashring R. Iyer,[1,3] Eric J. Chaney,[1] Carlos A. Renteria,[1,2] and Stephen A. Boppart[1,2,3,4,5,*]

[1]Beckman Institute for Advanced Science and Technology, University of Illinois Urbana-Champaign, Urbana, Illinois, 61801, USA
[2]Department of Bioengineering, University of Illinois Urbana-Champaign, Urbana, Illinois, 61801, USA
[3]Department of Electrical and Computer Engineering, University of Illinois Urbana-Champaign, Urbana, Illinois, 61801, USA
[4]Interdisciplinary Health Science Institute, University of Illinois Urbana-Champaign, Urbana, Illinois, 61801, USA
[5]NIH/NIBIB P41 Center for Label-free Imaging and Multiscale Biophotonics, University of Illinois Urbana-Champaign, Urbana, Illinois, 61801, USA
*boppart@illinois.edu

Received 28 February 2024; revised 28 March 2024; accepted 28 March 2024; posted 1 April 2024; published 1 May 2024

Hyperspectral coherent Raman scattering microscopy provides a significant improvement in acquisition time compared to spontaneous Raman scattering yet still suffers from the time required to sweep through individual wavenumbers. To address this, we present the use of a pulse shaper with a 2D spatial light modulator for phase- and amplitude-based shaping of the Stokes beam to create programmable spectrally tailored excitation envelopes. This enables collection of useful spectral information in a more rapid and efficient manner.

https://doi.org/10.1364/OL.521864

Introduction. Coherent Raman scattering (CRS), such as coherent anti-Stokes Raman scattering (CARS) and stimulated Raman scattering (SRS), provides significantly higher signal than spontaneous Raman scattering while maintaining signal integrity and is thus well suited for biomedical microscopy [1–5]. To collect hyperspectral (HS) data, the instantaneous frequency difference between the pump and Stokes beams is sequentially scanned to acquire one image per wavenumber. This time for spectral sweeping significantly limits the speed of HS image acquisition. Broadband CARS methods using a spectrometer are also used; however, these are slow due to the microsecond spectrum acquisition time, which is about 10^3 times longer than the traditional pixel dwell time in spectral sweeping [1]. Commonly, spectral sweeping is achieved by spectral focusing: the temporal delay between the linearly chirped pump and Stokes beams is scanned by tuning the relative optical path length difference using a motorized stage, thus scanning the instantaneous frequency difference of the two beams [6]. Additionally, spectral sweeping can be achieved by rapid wavelength tuning with narrowband beams. While these methods produce reliable results, they lack customizability and are limited to collecting one single narrow spectral window at a time.

Various methods have been developed to enable rapid collection of HS information. Pulse shaping methods were used for spectral sweeping and creation of binary spectral excitation masks in CARS [7] and SRS [8] using spatial light modulators (SLMs) and in SRS using a scanned slit [9]. Spectrally tailored excitation (STE)-SRS with a polarization shaping SLM and a Pockels cell enabled MHz modulation between two custom excitation spectra [10]. Additionally, sparse spectral sampling has been implemented in SRS [11] and CARS [12] to improve acquisition efficiency. Sparse sampling methods are possible because often the most useful HS information can be reduced to a set of specific wavenumbers with a much lower rank than the original data. Another method for multiplexed SRS encoded different wavenumbers with wavelength-specific frequency modulation [13]. Pulse shaping with SLMs has also been used to shape pump, Stokes, and probe pulses from a single original pulse in CARS [14,15].

Additionally, digital micromirror devices have been used as a binary modulator for the emitted broadband light from SRS [16] and spontaneous Raman [17] for compressed sensing. Including spectral selection in both excitation and emission, Lu *et al.* selected multiple Stokes wavelengths with a pulse shaper and spectrally separated these bands after emission to simultaneously collect three wavenumber regions [18]. The modulation of the emitted signal results in loss due to the inherent lossy nature of optical components and the intentional selective blocking of the signal and results in excess excitation on the sample which can cause photodamage. Other methods have been used in post-processing of HS data, such as independent component analysis [19,20], PCA [19], and phasor analysis [21,22] but still require lengthy HS acquisition times.

The aforementioned implementations yielded promising results yet lacked comprehensive excitation pulse programmability. Here, we present the use of a Fourier transform pulse shaper equipped with a 2D SLM for simultaneous phase and amplitude pulse shaping for programmable excitation in CARS microscopy. This enables customization of a HS excitation envelope via amplitude selection and optimization of the temporal overlap of the two excitation beams via phase shaping, which can be tailored for specific samples with *a priori* spectral information or used for adjusting the SNR, acquisition time, and/or spectral resolution of the system without *a priori* spectral information. This tunable excitation scheme of spectrally tailored

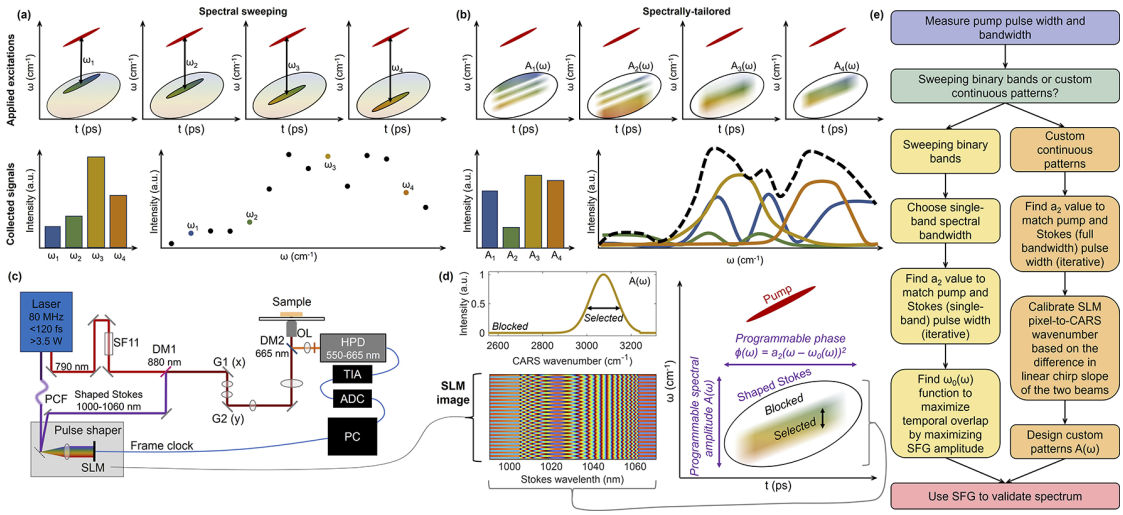

Fig. 1. Overview of spectrally tailored CARS. (a) In spectral sweeping, the instantaneous energy difference between the pump and Stokes is equal due to their matched linear chirps. This difference is tuned to sequentially acquire distinct vibrational energies (ω). Each pixel of a HS image has one intensity value for each measured individual wavenumber. (b) In spectrally tailored CARS, HS-CARS envelopes ($A(\omega)$) are applied via shaping the Stokes beam, and one intensity value is recorded for each of the excitation envelopes for each pixel within the image. (c) System diagram, including pulse shaper and SLM. (d) Example of applied CARS envelope $A(\omega)$, corresponding the SLM pattern applied to the Stokes beam, and time-frequency plot of the excitation. (e) Flowchart of how SLM patterns were created for spectrally tailored CARS. PCF, photonic crystal fiber; SLM, spatial light modulator; DM, dichroic mirror; G, galvo; OL, objective lens; HPD, hybrid photodetector; TIA, transimpedance amplifier; ADC, analog-to-digital converter.

CARS involves the use and creation of customized continuous HS excitation envelopes to enable more rapid and efficient collection of useful information (Fig. 1(b)) compared to the traditional spectral sweeping (Fig. 1(a)).

Methods. The system (Fig. 1(c)) was previously described by Yang *et al.* [7] for HS sweeping using phase- and amplitude-based pulse shaping in temporally optimized and spectrally shaped (TOSS) HS-CARS. Briefly, the system used a dual output (1045 and 790 nm) 80 MHz laser (InSight X3+, Spectra-Physics) along with a photonic crystal fiber (LMA-PM-10, NKT Photonics) to generate a supercontinuum Stokes beam (200 nm base-to-base). The central region of the supercontinuum (1000–1060 nm) was shaped with a Fourier transform pulse shaper using a 1920×1200 pixel 2D SLM (SLM 200, Santec). Due to the linear dependence of CARS intensity on the Stokes intensity, shaping the Stokes beam was selected. Images of 400×400 pixels were acquired with a 3.2 µs pixel dwell time and 5.76 s per frame. A 1.05 NA water immersion objective was used (XLPLN25XWMP2, Olympus). A 665 nm dichroic (FF665-Di02-25 × 36, Semrock) was used to separate the excitation from the epi-directed CARS signal, which additionally passed through a short pass and a bandpass filter (FF01-665/SP-25, FF01-665/150-25, Semrock). Photon counts were determined via computational photon counting using a hybrid photodetector (R10467U-40, Hamamatsu) [23]. Power on the sample was 10–30 mW for the pump beam and <6 mW for the Stokes beam; the pulse width at the sample plane was 850 fs for the pump, and the temporal profile of the Stokes was shaped to match 850 fs by modifying the quadratic coefficient of the SLM phase mask (Fig. 1(e), Fig. S1).

Various sets of SLM patterns were generated to shape the Stokes beam for customized excitation (Fig. 1(d)). Amplitude selection was achieved by applying horizontal lines orthogonal to the wavelength axis on the SLM to create destructive interference in the far field (Fig. S2). These patterns included higher (spectral) resolution spectral sweeping (Fig. S3), lower (spectral) resolution/higher SNR spectral sweeping (Fig. S4), Fourier series components (Fig. S5), and customized patterns tailored using *a priori* spectral information (Fig. S6). Higher-resolution spectral sweeping patterns were generated by tailoring spectral bands of the Stokes beam to have the same spectral bandwidth and pulse width as the pump beam, thus ensuring the same linear chirp [7], and were assumed to be the ground-truth CARS spectrum (Fig. S7). Lower-resolution/higher-SNR patterns were generated by selecting a spectral band twice as large as the high-resolution patterns and a pulse width that matches the pump to optimize power efficiency on the sample and excite a broader wavenumber region using the mismatch of the linear chirps, thus exciting more overall CARS signal.

Other customized patterns were generated by producing a broadband Stokes beam with the same pulse width as the pump (Fig. S1) and shaping the amplitude within that band by varying the intensity of horizontal lines (Fig. S2). Patterns were validated with sum-frequency generation spectra at the sample plane (Figs. S3–S6) using a spectrometer (USB4000, Ocean Optics), with a measured full-width at half-maximum at 450 nm of ~2 nm. The limited spectral resolution after conversion to wavenumber (100 cm^{-1}, Fig. S8) of the spectrometer limits the ability to validate higher spectral frequencies.

Results and discussion. First, samples of two different types of beads were examined to observe system capabilities for differentiating and segmenting two chemically distinct substances. Pure samples of polystyrene (PS) or polymethyl-methacrylate (PMMA) beads (1 µm diameter) were characterized with higher-resolution spectral sweeping to determine the CARS signatures of the two beads (Fig. 2(a)), matching previously acquired spectra [20]. From these pure spectra, two binary masks were designed to selectively excite PMMA (spectral excitation 1)

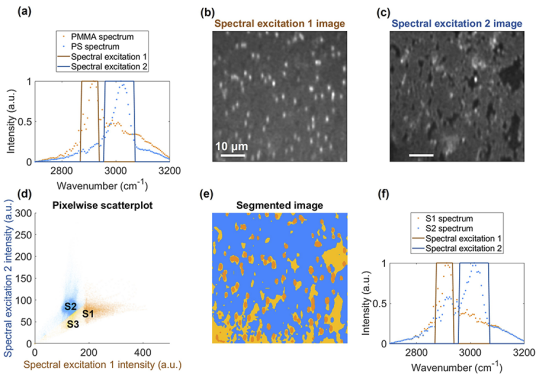

Fig. 2. Differentiation of PMMA and PS beads using two tailored spectral masks. (a) CARS spectrum from pure samples of each type of bead, along with custom masks design to specifically excite each type of bead. Images acquired from a mix of PS and PMMA beads using (b) Mask 1 and (c) Mask 2. (d) Scatterplot of pixelwise intensities of Mask 2 versus Mask 1, along with segmentation into three different spectral signatures (S1, S2, S3). (e) Image showing pixels corresponding to the spectral signatures in (d). (f) HS-CARS data collected on the same FOV, displaying the spectra of segmented regions S1 and S2 in (e).

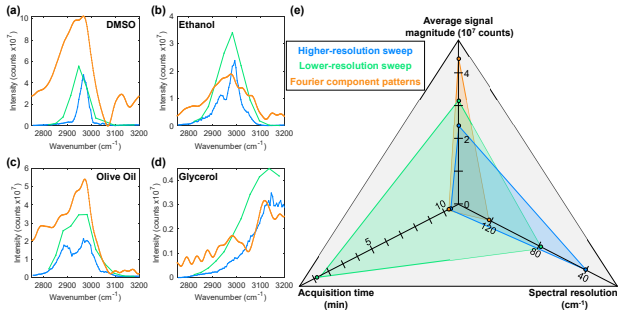

Fig. 3. Four substances imaged with different tailored excitation schemes: higher-resolution sweep (101 narrow patterns, 42 cm^{-1} spectral resolution), lower-resolution sweep (11 broad patterns, 78 cm^{-1} spectral resolution), and Fourier components (100 sine patterns with different phase shifts and frequencies). All three schemes were used to image pure solutions of (a) DMSO, (b) ethanol, (c) olive oil, and (d) SF57 glass for the non-resonant background. (e) Quantification of the trade-offs of collected CARS signal magnitude (calculated as the difference between maximum and minimum spectral intensities), the spectral resolution (calculated as the FWHM of DMSO peak), and the acquisition time.

and PS (spectral excitation 2). These custom spectral excitation envelopes were applied via the SLM to image a mixture of PS and PMMA beads. The mixture was also imaged with the set of higher-resolution sweeping patterns for validation. Images acquired using the custom spectral excitation envelopes (Figs. 2(b) and 2(c)) selectively highlighted subsets of beads. The pixelwise intensities from the two custom spectral excitation envelopes were visualized on a scatterplot (Fig. 2(d)) and used to segment three different regions: S1 (high spectral excitation 1 intensity), S2 (high spectral excitation 2 intensity), and S3 (background). The set of higher-resolution sweeping patterns was also acquired on the same FOV, and spectra from segmented regions S1 and S2 (Fig. 2(f)) matched well with the original PMMA and PS pure spectra (Fig. 2(a)), indicating that the custom pair of spectral excitation envelopes can be used for the segmentation of the two bead types with ~1/50 total acquisition time of the spectral sweeping (2 patterns × 5.76 s = 11.52 s versus 101 patterns × 5.76 s = 581.76 s) and with 84% of PMMA pixels and 97% of PS pixels classified in agreement with using the higher-resolution patterns for segmentation (Fig. S9), likely with decreased accuracy due to a small shift in the focal plane during the higher-resolution spectral sweep.

Next, the tunability of acquisition time, spectral resolution, signal magnitude, and SNR capabilities were examined. Three sets of excitation spectra were used: higher-resolution spectral sweeping (Fig. S3), lower-resolution spectral sweeping (Fig. S4), and Fourier patterns (Fig. S5). The patterns were used to image DMSO, ethanol, and olive oil, along with the non-resonant background from the SF57 glass (Fig. 3). As expected, the set of 11 lower-resolution patterns provided improved signal magnitude compared to the higher-resolution sweep due to the increased CARS generated from the larger spectral window (Fig. 3). Due to the loss throughout the system, the maximum power of the shaped Stokes beam on the sample for one of the higher-resolution patterns is ~3 mW, which increases to ~6 mW with the lower-resolution patterns. By shortening the overall acquisition time with the lower-resolution pattern set, the contribution of dark counts to the overall signal is decreased, further improving the SNR. Often, higher spectral resolution is favorable; however, in scenarios where fast acquisition is essential, customized patterns can be created to have the broadest acceptable spectral bandwidth, maximum SNR, and fastest acquisition by programming the spectral bandwidth and chirp of the pulses for spectral sweeping; e.g., the demonstrated lower-resolution sweep (11 patterns) was acquired ~9 times faster than the higher-resolution sweep (101 patterns) and provides useful spectral information (Fig. 3(e)). Sacrificing spectral resolution for faster imaging has previously been performed, such as by Suzuki *et al.* who created a 4-color SRS flow cytometer [24] and Bae *et al.* who used binary spectral masks in SRS microscopy [8].

The Fourier component basis (100 patterns), inspired by spectral phasor analysis [25], improved the signal magnitude for some samples and somewhat matched the shapes of the expected spectra. However, the spectra showed unexpected modulations, likely due to reconstruction errors , which could be affected by higher-order dispersion of the overall microscope. In future work, higher-order dispersion compensation could be calibrated for sets of patterns and applied as part of the phase masks using the SLM. The trade-off between spectral resolution, acquisition time, and signal magnitude for the three tested sets of patterns is quantified in Fig. 3(e). While the signal magnitude was the highest for the Fourier series components (4.4×10^7 counts) compared to the lower-resolution (3.1×10^7 counts) and higher-resolution (2.3×10^7 counts) sweeps, when SNR was calculated as the mean ratio of the maximum value and the mean of a silent region from 3100 to 3200 cm^{-1}, the lower-resolution sweep provided the best SNR (95.5) compared to the higher-resolution sweep (64.0) and the Fourier component (9.9).

Ex vivo murine abdominal adipose tissue was imaged (Fig. 4), motivated by the known Raman signature of lipids. All animal procedures were conducted in accordance with a protocol approved by the Institutional Animal Care and Use Committee (IACUC) at the University of Illinois Urbana-Champaign. To retrieve the *ex vivo* tissue, a mouse was euthanized by CO_2

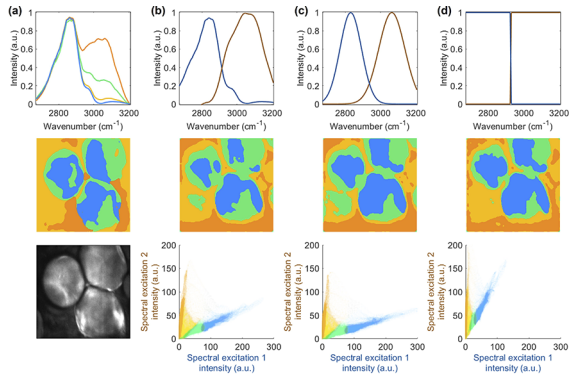

Fig. 4. Spectrally tailored CARS of adipocytes. (a) Overall CARS intensity of adipocytes, customized segmented regions based on high-resolution swept HS-CARS, and CARS spectra of different segmented spatial components. Different spectral excitation envelopes were applied: (b) spectral components, (c) Gaussians, (d) binary masks.

asphyxiation and cervical dislocation, and a piece of skin was removed, including subcutaneous fat. First, higher-resolution spectral sweeping was acquired on a FOV (Fig. 4(a)), and four regions with similar spectra were segmented, two intra-adipocyte components (blue and green), and two extra-adipocyte components (yellow and orange). Multiple new pairs of excitation spectral envelopes were tailored and applied to the SLM for imaging (Figs. S6 and S10) based on the normalized spectra from the segmented blue region and the difference between the segmented blue and orange regions (Fig. 4(b)), Gaussian fits to these spectra (Fig. 4(c)), and binary masks (Fig. 4(d)). Images were segmented to highlight similar regions based on manual tuning of linear boundaries between segmented areas in the pixelwise scatterplot; K-means clustering additionally yielded segmentation results (Fig. S11).

This work presents a proof of concept for spectrally tailoring CRS microscopy with programmable phase and amplitude and could be expanded in a variety of ways to improve performance and scope. While this study focused on the CH region (~2700–3200 cm^{-1}), future work could examine the feasibility of this approach in the fingerprint region, widely used due to its specificity for biomedical imaging, yet can present a challenge due to the lower signal intensity compared to the CH region. Furthermore, advanced methods for spectral decomposition and analysis could better define spectral basis functions, such as independent component analysis [20] or weakly supervised learning [26]. Thus, spectrally tailored excitation provides immense utility for improving acquisition and processing efficiency in well-defined HS imaging tasks, while high-resolution spectral sweeping will likely remain the standard for discovery-based imaging tasks. Conveniently, the system setup for spectrally tailored CARS is compatible with spectral sweeping. In this work, the impact of the CARS non-resonant background is reduced by the longer pulse widths and the epi-detection geometry [27]. In future work, the non-resonant contribution could be avoided by alternative pulse shaping methods [10,14,28], such as temporally delaying a probe pulse with a different wavelength than the pump [14,28].

Conclusion. Collecting massive, low rank HS dataset requires unnecessarily long acquisition/processing times. Here, we presented a method for programmable spectral tailoring of the Stokes beam in CARS microscopy using a Fourier transform pulse shaper in order to achieve precise control over spectral excitation envelopes, enabling adaptable spectral resolution, SNR, and acquisition time. This method enables the user to collect only the essential spectral information and optimizes the acquisition process.

Funding. National Institutes of Health (P41EB031772, R01CA213149, R01CA241618, T32EB019944).

Acknowledgment. The authors would like to acknowledge Darold Spillman Jr. for his administrative and technical support. Additional information can be found at: http://biophotonics.illinois.edu.

Disclosures. An invention disclosure has been submitted for the technique to perform temporal optimization and spectral shaping for hyperspectral microscopy (L.Y., J.E.S., R.R.I., and S.A.B.). The authors declare that they have no other competing interests.

Data availability. Data underlying the results presented in this paper are not publicly available at this time but may be obtained from the authors upon reasonable request and through a collaborative research agreement.

Supplemental document. See Supplement 1 for supporting content.

REFERENCES

1. C. Zhang, D. Zhang, and J. X. Cheng, Ann. Rev. Biomed. Eng. **17**, 415 (2015).
2. C. W. Freudiger, W. Min, B. G. Saar, *et al.*, Science **322**, 1857 (2008).
3. C. L. Evans, E. O. Potma, M. Puoris'haag, *et al.*, Proc. Natl. Acad. Sci. U.S.A. **102**, 16807 (2005).
4. J. X. Cheng and X. S. Xie, J. Phys. Chem. B **108**, 827 (2004).
5. A. A. Fung and L. Shi, WIREs Syst. Biol. Med. **12**, e1501 (2020).
6. T. Hellerer, A. M. K. Enejder, and A. Zumbusch, Appl. Phys. Lett. **85**, 25 (2004).
7. L. Yang, R.R. Iyer, J.E. Sorrells, *et al.*, "Temporally-optimized spectrallyshaped hyperspectral coherent anti-Stokes Raman scattering microscopy," Opt. Express, in press (2024).
8. K. Bae, W. Zhang, and Z. Huang, Theranostics **10**, 312 (2020).
9. D. Zhang, P. Wang, M. N. Slipchenko, *et al.*, Anal. Chem. **85**, 98 (2013).
10. C. W. Freudiger, W. Ming, and G. R. Holtom, Nat. Photonics **5**, 103 (2011).
11. I. J. Pence, B. A. Kuzma, M. Brinkmann, *et al.*, Biomed. Opt. Express **12**, 6095 (2021).
12. F. Masia, P. Borri, and W. Langbein, Opt. Express **22**, 4021 (2014).
13. D. Fu, F.-K. Lu, X. Zhang, *et al.*, J. Am. Chem. Soc. **134**, 3623 (2012).
14. L. Brückner, T. Buckup, and M. Motzkus, J. Opt. Soc. Am. B **33**, 1482 (2016).
15. N. Dudovich, D. Oron, and Y. Silberberg, Nature **418**, 512 (2002).
16. P. Berto, C. Scotté, F. Galland, *et al.*, Opt. Lett. **42**, 1696 (2017).
17. D. S. Wilcox, G. T. Buzzard, B. J. Lucier, *et al.*, Anal. Chim. Acta **755**, 17 (2012).
18. F.-K. Lu, M. Ji, D. Fu, *et al.*, Mol. Phys. **110**, 1927 (2012).
19. H. Mitsutake, S. R. Castro, E. de Paula, *et al.*, Int. J. Pharm. **552**, 119 (2018).
20. Y. Ozeki, W. Umemura, Y. Otsuka, *et al.*, Nat. Photonics **6**, 845 (2012).
21. H. J. Braddick, W. J. Tipping, and L. T. Wilson, Anal. Chem. **95**, 5369 (2023).
22. D. Fu and X. S. Xie, Anal. Chem. **86**, 4115 (2014).
23. J. E. Sorrells, R. R. Iyer, L. Yang, *et al.*, ACS Photonics **9**, 2748 (2022).
24. Y. Suzuki, K. Kobayashi, Y. Wakisaka, *et al.*, Proc. Natl. Acad. Sci. U. S. A. **116**, 15842 (2019).
25. F. Fereidouni, A. N. Bader, and H. C. Gerrison, Opt. Express **20**, 12729 (2012).
26. J. Shi, K. Bera, P. Mukherjee, *et al.*, Anal. Chem. **95**, 10957 (2023).
27. J.-X. Cheng, Y. K. Jia, G. Zheng, *et al.*, Biophys. J. **83**, 502 (2002).
28. D. Oron, N. Dudovich, D. Yelin, *et al.*, Phys. Rev. A **65**, 043408 (2002).